

5th International Conference on Silicon Photovoltaics, SiliconPV 2015

Short-circuit current density imaging methods for silicon solar cells

Fabian Fertig^{a*}, Milan Padilla^a, Otwin Breitenstein^b, Hannes Höffler^a, Ino Geisemeyer^a,
Martin C. Schubert^a, Stefan Rein^a

^aFraunhofer Institute for Solar Energy Systems, Heidenhofstr. 2, D-79110 Freiburg, Germany

^bMax Planck Institute of Microstructure Physics, Weinberg 2, D-06120 Halle, Germany

Abstract

Recently, several novel methods have been proposed to image short-circuit current density j_{sc} based on diverse physical principles. This work compares these methods and points out physical limitations, advantages and drawbacks of each approach. One method based on photoluminescence (PL) imaging and two methods based on dark and illuminated lock-in thermography (DLIT / ILIT) are discussed. As a versatile reference technique for j_{sc} mapping, spectrally-resolved light-beam induced current (SR-LBIC) is applied. Experimental results for crystalline silicon solar cells with varying substrate properties, rear-side passivation schemes and process-induced defects are presented. Investigated parameters are quantitative accuracy of local j_{sc} , spatial resolution, measurement time, spectral excitation dependency and calibration. Furthermore, robustness towards locally increased series resistance R_s and injection-dependent recombination is discussed along with proneness to artefacts due to local shunts, spatially varying optics and photogeneration, and fitting algorithm artefacts.

© 2015 The Authors. Published by Elsevier Ltd. This is an open access article under the CC BY-NC-ND license (<http://creativecommons.org/licenses/by-nc-nd/4.0/>).

Peer review by the scientific conference committee of SiliconPV 2015 under responsibility of PSE AG

Keywords: Short-circuit current; imaging; photoluminescence; lock-in thermography

1. Introduction

It has been shown [1–3] that, especially in solar cells made from multicrystalline silicon (mc-Si), short-circuit current density j_{sc} can vary significantly across the cell and even limit local conversion efficiency η_{xy} [3]. Since the

* Corresponding author. Tel.: +49-761-4588-5482; fax: +49-761-4588-9250.

E-mail address: fabian.fertig@ise.fraunhofer.de

latest proposed methods calculating η_{xy} from extracted diode parameters [4,5] assume j_{sc} to be constant, the spatially resolved determination of j_{sc} on solar cell level is expected to be highly beneficial for local solar cell analysis.

The objective of this work is to compare the physics of four different methods to extract maps of j_{sc} in theory and by experiment. These four methods are based on (i) photoluminescence (PL) imaging [6], (ii) illuminated [7] (ILIT) and (iii) dark (DLIT) lock-in thermography [8], and (iv) spectrally-resolved light-beam induced current (SR-LBIC) [2], all published by authors of this work.

2. Investigated methods and experimental setup

In the following, the working principles and underlying physics of each method are discussed, along with important technical details on the experimental setups.

2.1. Photoluminescence (PL)

PL signal is proportional to the product of charge carrier densities: $S_{PL} \sim n_{xy} p_{xy} \sim \exp(V_{xy})$, and, therefore, the splitting of the quasi-Fermi levels (\triangleq voltage V) rather than current density j . By assuming the charge carriers in the bulk to dominate PL signal and considering the diffusion of minority charge carriers from the bulk to the space charge region (see blue arrows in Fig. 1a) by a variable “diffusion resistance”, an alternative one-diode model has been proposed [9]. This model assigns an implied voltage V_{imp} in the bulk to the splitting of the quasi-Fermi levels which is larger than the pn junction voltage V_{pn} , which is typically considered in PL evaluation. In contrast to previous approaches of imaging diode model parameters via PL [4,10–12], the diffusion-limited carriers, meaning the carriers that are not extracted under SC conditions due to non-ideal internal quantum efficiency, are not corrected for but explicitly considered. By introducing an additional diode model parameter $j_{DL} = j_{gen} - j_{sc}$ for the difference between photo-generated and extracted short-circuit current density, the diffusion-limited carriers are considered in defining a set of equations for diode model parameter extraction [6,13]. This set of equations is iteratively solved to extract parameter values, while assuming low-level injection to hold in all four acquired images. With the assumption of spatially homogeneous j_{gen} , a spatially resolved image of j_{sc} can be calculated [6,13]. The luminescence setup applied within this work features a laser diode with a wavelength of $\lambda = 790$ nm for illumination and a one megapixel silicon CCD camera.

2.2. Illuminated lock-in thermography (ILIT)

Lock-in thermography (LIT) images can be scaled to local power dissipation [14]: $S_{LIT} \sim p_{xy} \sim j_{xy} V_{xy}$. The basic idea of the ILIT-based method [7] is to exploit the property of crystalline silicon solar cells that the illuminated current density under moderate reverse bias V_{rev} , i.e. well before junction breakdown sets in, does not differ significantly from j_{sc} . This is done by recording a difference ILIT image between short-circuit (SC) and V_{rev} . Fig. 1 illustrates selected thermal power contributions to the detected ILIT signal under SC and V_{rev} conditions. For both conditions, the constant contributions p_{th} due to thermalization of generated carriers to the band edges as well as the current-driven (for $V_{pn} \leq 0$ V) contributions p_{rec} (recombination), p_{pelt} (Peltier heating/cooling at metal contacts), p_s (series resistance, not shown in Fig. 1) exhibit the same values. By recording a difference image, they should cancel out. The only two contributions left are (i) thermalization across the pn junction p_{pn} , which is proportional to current and voltage and (ii) parallel (shunt) resistance p_p (not shown in Fig. 1). Hence, manipulating p_{pn} is the main mechanism of the ILIT-based method to extract local j_{sc} , while p_p leads to artefacts in areas of local shunting. These artefacts can be corrected by recording an additional DLIT image. Hence, in contrast to the PL-based method, the ILIT-based method does not rely on a diode model. The LIT images used for this method are recorded with two commercially available LIT systems with a lock-in frequency of $f_{lock-in} = 40$ Hz. The cameras of both systems used in this work feature Stirling-cooled InSb FPA detectors with a resolution of 256×256 pixels (system 1) and 512×512 pixels (system 2) and are sensitive in the mid-infrared wavelength range. During ILIT, the cells are illuminated with a laser diode at $\lambda = 940$ nm (system 1) or LED arrays at selectively $\lambda = 470$ nm, 640 nm or 940 nm (system 2).

Throughout this work, system 1 has been applied except for the spatially- and spectrally-resolved considerations in sections 3.3 and 3.4, respectively.

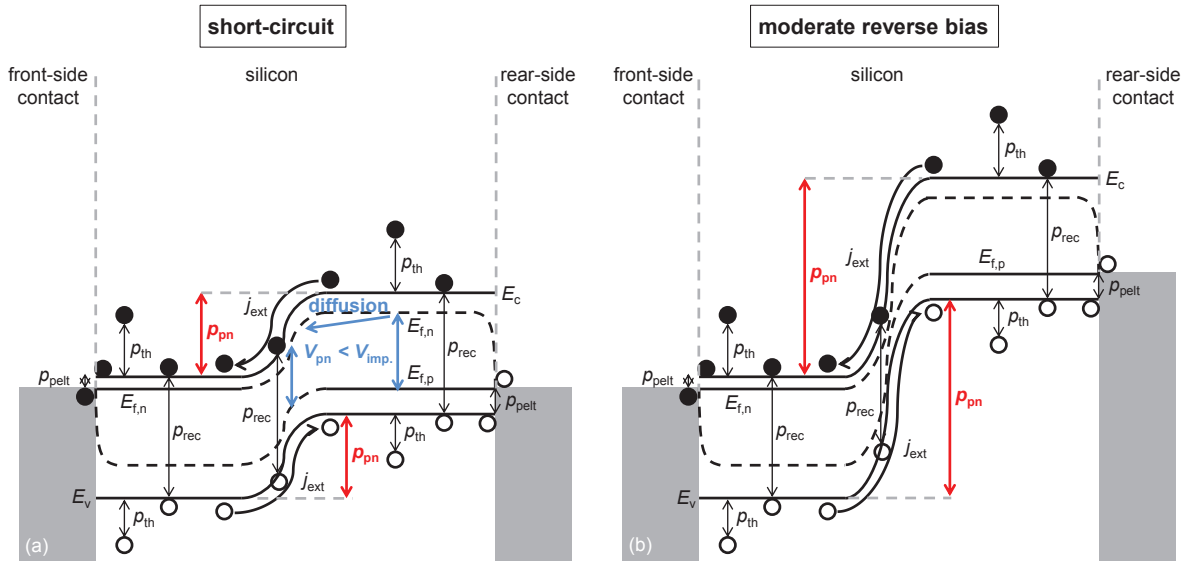


Fig. 1. Band diagram sketches of a Si solar cell under (a) short-circuit and (b) moderate reverse bias with indicated heating contributions. In (a) the difference between p_n junction voltage V_{pn} and implied bulk voltage V_{imp} due to minority charge carrier diffusion is indicated. Band diagrams are adapted from Ref. [15].

2.3. Dark lock-in thermography (DLIT)

The underlying idea of the DLIT-based j_{sc} imaging method is to derive an empirical expression to correlate the dark saturation current density j_{01} of the one-diode model of a solar cell to j_{DL} [8]. Based on PC1D simulations, the expression $j_{DL} = A \cdot j_{01} - B \cdot j_{01}^2 - C$ is derived, with A , B , C being empirical fit parameters [8]. These fit parameters can be determined by simulation or a fit to a reference method [8] and an image of j_{01} can be derived from a series of DLIT images [16]. If these DLIT images are recorded at moderate currents, the assumption of a homogeneous lumped series resistance is generally sufficient. By assuming a laterally homogeneous photo-generated current density j_{gen} , the local short-circuit current density can be derived via $j_{sc,xy} = j_{gen} - j_{DL,xy}$. If the global short-circuit current density value $j_{sc,tot}$ rather than j_{gen} is known (still assuming laterally homogeneous photo-generation), the two previous equations can be combined, eliminating fit parameter C . The empirical expression to correlate local j_{sc} to j_{01} is then given by $j_{sc,xy} = j_{sc,tot} + 1/N \cdot \sum (A \cdot j_{01} - B \cdot j_{01}^2) - A \cdot j_{01} + B \cdot j_{01}^2$ [8], with N being the number of pixels. Although being purely empirical, the appeal of the DLIT-based j_{sc} imaging method is that – once properly calibrated to a certain cell type and material – it should improve the local efficiency analysis based on DLIT [5] without the need to record further images. The images presented within this work are recorded with $f_{lock-in} = 10$ Hz using system 2 described in section 2.2.

2.4. Light-beam induced current (LBIC)

The most direct way of measuring local j_{sc} is by LBIC [17–19]. For this purpose, a light-beam is focused to a spot and scanned over the short-circuited solar cell under test. The locally induced current can be scaled to external quantum efficiency EQE by an additional spectral response measurement. From this, a value of local j_{sc} can be determined for a given photo-current density j_{ph} . Hence, the measured LBIC signal is directly proportional to local

j_{sc} : $S_{LBIC} \sim j_{sc,xy}$. By using light sources with differing excitation wavelengths λ , spectrally-resolved (SR-) LBIC maps can be generated [1,20]. By interpolation in-between the nodes of the local EQE at different wavelengths, maps of j_{sc} for arbitrary spectra, e.g. AM1.5G, can be derived by spectral integration, taking into account the full range of λ -dependent effects [2]. The LBIC maps presented within this work have been recorded with a commercially available measurement system featuring laser diodes with wavelengths of $\lambda = 405, 532, 670, 780, 940$ and 1060 nm that run simultaneously with Gaussian intensity profiles and FWHM of $150\text{--}200$ μm . The system does not feature a bias light and therefore operates under very low injection.

3. Experimental results and discussion

The investigated j_{sc} imaging methods have been applied on four large-area ($A_{\text{cell}} = 15.6 \times 15.6$ cm^2) p -type silicon solar cells with screen-printed metallisation, manufactured on industrial mass-production equipment at Fraunhofer ISE. Cell 1 constitutes a standard mc-Si aluminium back-surface-field (Al-BSF) cell and cell 2 a cast-mono Si passivated emitter and rear (PERC [21]) cell with thermal-oxide passivated front and rear sides [22] and laser-fired contacts [23]. Cells 3 and 4 are PERC cells from neighbouring mc-Si substrates – cell 3 constituting the same cell structure as cell 2 and cell 4 applying a plasma-enhanced chemical vapour deposited (PECVD) aluminium oxide [24] for rear-side passivation. Each passivation layer is capped by PECVD silicon oxide and / or silicon nitride. Characteristic j - V parameters for all cells, measured with an industrial flasher-based cell tester, are given in Tab. 1. Note that the Al-BSF cell has been processed in 2014 while the PERC cells date back to 2011 and 2012.

Table 1. Characteristic j - V parameters of the investigated solar cells for illumination with the AM1.5G spectrum: efficiency η , open-circuit voltage V_{oc} , short-circuit current density j_{sc} , short-circuit current I_{sc} , fill factor FF , pseudo fill factor pFF , parallel resistance R_p and series resistance R_s

Cell	η (%)	V_{oc} (mV)	j_{sc} (mA/cm ²)	I_{sc} (A)	FF (%)	pFF (%)	R_p (Ωcm^2)	R_s (Ωcm^2)
1 – mc-Si, Al-BSF	17.0	621	34.9	8.50	78.1	81.1	14×10^3	0.7
2 – cast-mono, PERC SiO ₂	19.2	646	38.7	9.42	76.7	82.2	59×10^3	1.0
3 – mc-Si, PERC SiO ₂	17.1	627	35.0	8.52	77.7	81.5	16×10^3	0.8
4 – mc-Si, PERC Al ₂ O ₃	17.2	628	35.3	8.60	77.5	81.7	7×10^3	0.8

3.1. Calibration and visual comparison

Figs. 2 and 3 show the results for imaging the local j_{sc} of cell 1 (Al-BSF) with the four introduced methods. The LBIC map recorded at $\lambda = 940$ nm and shown in Fig. 2 is scaled to local j_{sc} by adjusting its integral value to equal the measured current I_{sc} during ILIT at SC. Since thermal diffusion significantly blurs LIT images, the LBIC map is blurred for better comparability. This is done by assuming the LBIC map to correlate to a power source image and by emulating thermal diffusion by the respective point spread function comparable to the recording conditions during the LIT measurements. The ILIT j_{sc} image in Fig. 2 is scaled as described in section 2.2. One image is recorded pulsing the voltage between SC and $V_{rev} = -2$ V, which can be directly scaled to local j_{sc} [7], and ohmic shunts are corrected with an additional DLIT image recorded at the same V_{rev} . Emissivity correction is performed according to Ref. [25]. To generate the DLIT-based j_{sc} image, a j_{01} image has been derived following the procedure described in Ref. [16], with an input of three DLIT images recorded at $V = 0.55$ V, $V = 0.6$ V and $V = -1$ V (for ohmic shunt correction), and the assumption of a homogeneous series resistance of $R_s = 0.6$ Ωcm^2 . The empirical fit parameters are determined by adjusting them to an optimum fit of the resulting DLIT-based j_{sc} image to the blurred LBIC image. During j_{01} imaging, mean values of the surrounding areas are assigned to the busbars and, therefore, local j_{sc} is overestimated in these regions due to the assumption of a laterally constant photogeneration. Since this procedure impacts the implied global j_{sc} , the local j_{sc} values in the non-busbar regions would be derived as too low when using the same global j_{sc} value as for the other methods. Hence, its value is increased by a factor of ≈ 1.04 in order to be comparable with the other methods [8]. Fig. 2 shows good qualitative agreement between LBIC, ILIT-

and DLIT-based j_{sc} images. Regions of decreased local j_{sc} due to defects and dislocations agree well. As discussed, the busbars exhibit artificially increased values in the DLIT-based image. Fig. 2 (bottom) shows normalised histograms of the discussed images. The unblurred LBIC image shows the most narrow distribution with its peak occurring at higher j_{sc} values than for the LIT-based methods. When emulating the thermal diffusion occurring during LIT (blurring), this peak shifts closely to the ones originating from the ILIT- and DLIT-based methods. Furthermore, the distribution of the values is similar which confirms the good correspondence concerning contrast as visible in the images. In the histogram of the DLIT-based j_{sc} image, four pronounced peaks can be seen that stick out from the course of the curve. The two peaks occurring for $j_{sc} < 35 \text{ mA/cm}^2$ are due the described busbar effect and the first peak for $j_{sc} > 35 \text{ mA/cm}^2$ describes the area beyond the cell area, which has been set to a finite value. Hence, by optimizing the method and evaluation routine, it should be possible to eliminate these artefacts easily. The peak occurring at the highest j_{sc} value, however, represents actual artefacts of the method where the assumed empirical correlation between j_{01} and j_{DL} fails.

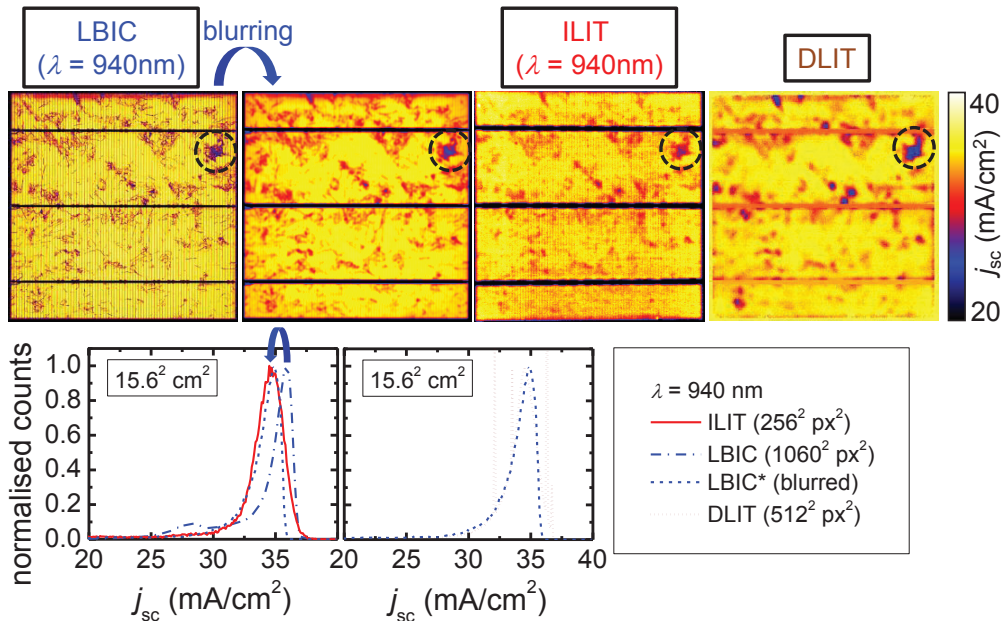


Fig. 2. Resulting j_{sc} images and according histograms of cell 1 (mc-Si Al-BSF) for LBIC and the ILIT- and DLIT-based methods. Circle = extended dislocation cluster.

Fig. 3 shows the result of the PL-based method for cell 1, along with an LBIC image recorded at $\lambda = 780 \text{ nm}$ which is the closest wavelength available to $\lambda = 790 \text{ nm}$ of the PL laser. The images are scaled more narrowly to be comparable in appearance to the images recorded at $\lambda = 940 \text{ nm}$, see Fig. 2. Also for PL, the resulting j_{sc} image qualitatively agrees with the LBIC map while the contrast appears smaller in the PL image. This is confirmed by the more narrow distribution of the histogram displayed in Fig. 3. As pointed out in Ref. [13], this lower contrast is due to the balancing currents across the emitter and metallisation grid, which equalize voltage difference in-between different areas of the cell [26,27] and contradict the underlying assumption of each pixel representing a de-coupled terminal-connected diode. This effect has been addressed recently by detailed simulations [28], revealing that the accuracy of PL-based j_{01} imaging in local low-lifetime regions, on which the PL-based j_{sc} imaging method is based on, is insufficient. Hence, the overall visual appearance of all j_{sc} images is comparable while the j_{sc} image resulting from the PL-based method exhibits a smaller contrast. Four PL images have been recorded as input [13] and the resulting image is scaled to the same I_{sc} as for the other images. Tab. 2 summarizes the required input parameters for each method to generate a calibrated j_{sc} image. It can be seen that only the ILIT-based method can be calibrated self-

consistently without the need of further information. However, the required additional information for the other methods can be gathered rather easily or needs to be determined only once for a specific cell architecture and substrate material.

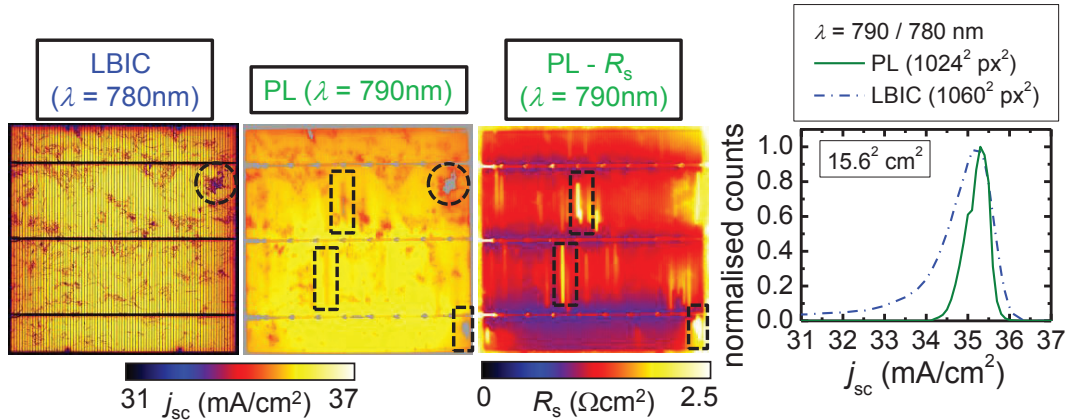


Fig. 3. Resulting j_{sc} images and according histograms of cell 1 (mc-Si Al-BSF) for LBIC and the PL-based method. Series resistance image has been derived from C-DCR [11]. Boxes \triangle areas of increased R_s . Circle = extended dislocation cluster. Grey \triangle divergent algorithm.

3.2. Robustness concerning locally increased series resistance and algorithm artefacts

Fig. 3 shows an image of local series resistance R_s for cell 1 determined by C-DCR [11]. Multiple regions with significantly increased values of local R_s can be seen. As indicated by the boxes, some of these regions lead to artefacts in the PL-based j_{sc} image, either by a virtual decrease in local j_{sc} or divergence of the entire iterative fitting algorithm, highlighted in grey. The LBIC maps and the LIT-based methods displayed in Fig. 2 show robust towards locally increased values of R_s . For LBIC, the cell is kept under SC and the resulting j_{sc} map should therefore be free from R_s artefacts. The measurement system applied during this work does not feature a bias light and, therefore, local illumination yields only comparably small currents. That is, even if local R_s is that high that it actually influences local j_{sc} under 1 sun illumination, this effect may remain undetected during LBIC without bias light [29]. For ILIT, the result is robust against locally increased R_s as long as the local illuminated current density under SC and V_{rev} does not differ significantly [15]. For the DLIT-based method, the j_{01} image determined by a series of DLIT images needs to be free of R_s artefacts. This can be achieved by recording all DLIT images at moderate currents or using a separate R_s image to correct for inhomogeneous voltage gradients across the cell [5]. In Figs. 2 and 3, an extended dislocation cluster with severely impacted local j_{sc} is marked by a circle. As can be seen in the PL-based j_{sc} image in Fig. 3, the iterative fitting algorithm also diverges in this region. Divergence issues of the PL-based method have been reported already in the original manuscripts [6,13]. In conclusion, the PL-based image appears to be most prone to artefacts due to the application of an iterative fitting algorithm. As discussed in section 3.1, the DLIT-based method suffers from minor artefacts as seen by the discussed highest pronounced peak in the histogram shown in Fig. 2.

Table 2. Required input parameters for discussed j_{sc} imaging methods. $f_{met} \triangleq$ metallisation fraction

Input	LBIC	ILIT	DLIT	PL
Number of required images (optional addition)	1 map per λ	1 (+ 1 for ohmic shunt correction) (+ ≤ 2 for emissivity correction)	2 to 3 (+ 1 for ohmic shunt correction) (+ ≤ 2 for emissivity correction) (+ 1 R_s image \rightarrow e.g. +2 EL images for RESI [30] or +4 lum. images for C-DCR [11])	4
Further parameters	$j_{sc,tot}$ OR EQE and j_{gen}	none	$j_{sc,tot}$ OR j_{gen} fit parameters A, B (and C) (lumped R_s)	f_{met}

3.3. Spatial resolution

Fig. 4 shows a zoom into the area of cell 1 containing the extended dislocation cluster marked with a circle in Figs. 2 and 3. The histogram within this dislocation cluster, see Fig. 4 (bottom), shows a close correlation between LBIC and the ILIT-based method with a similar contrast and distribution of significantly impacted regions. The according histogram of the DLIT-based method shows a pronounced peak with values of $j_{sc} < 25 \text{ mA/cm}^2$ that does not show within the other two methods. Since the DLIT-based j_{sc} image can be considered a re-scaled j_{01} image, see section 2.3, this peak represents areas within the dislocation cluster where the local j_{01} is impacted more by a decrease in charge carrier lifetime than the local j_{sc} according to the derived empirical correlation. This effect is discussed in more detail in Ref. [8]. Fig. 4 shows the same zoomed area for the PL-based image and the correlating LBIC image at $\lambda = 780 \text{ nm}$, again scaled to the same appearance as the images for $\lambda = 940 \text{ nm}$. In accordance with the behaviour for the entire cell, the decrease in local j_{sc} is significantly less pronounced in the PL-based j_{sc} image as can be seen in other dislocated areas beneath the extended dislocation cluster discussed before.

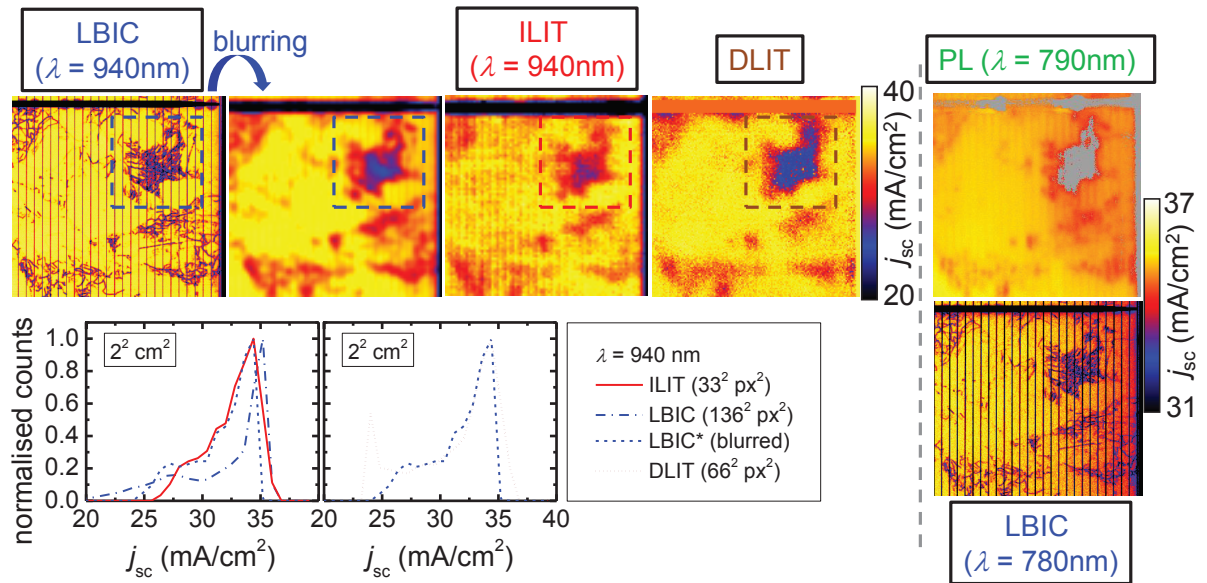


Fig. 4. Zoom into the area containing the extended dislocation cluster marked in Figs. 2 and 3.

The LBIC maps displayed in Figs. 2 to 4 show a significantly higher resolution than the LIT-based and PL-based images. As mentioned before, the spatial resolution of LIT imaging is limited by the thermal diffusion length, which is proportional to $1/\sqrt{f_{lock-in}}$ [14], with $f_{lock-in}$ being the applied lock-in frequency. Fig. 5 shows ILIT-based j_{sc} images of the zoomed area recorded at different $f_{lock-in}$. In this case, one image only has been recorded and no shunt correction has been applied, which leads to the point source artefact in the top left part of the ILIT images due to local shunting. Due to the $1/\sqrt{f_{lock-in}}$ dependency, coming from low $f_{lock-in}$ the spatial resolution first improves significantly while its improvement slows for higher $f_{lock-in}$. However, when comparing the image recorded at $f_{lock-in} = 190 \text{ Hz}$, which is close to the currently technically feasible limit, with the unblurred LBIC image, a close correlation can be seen. This is further illustrated by the two height profiles of the dislocation cluster depicted in Fig. 5, showing local peaks within the dislocation cluster and local minima at the location of the contact fingers. When considering the 0° image of the same measurement, see Fig. 5 below the 190 Hz image, a sharp image of the local j_{sc} can be seen. Deconvolution of thermally blurred LIT images [14] has the potential to improve the spatial resolution of these images even more. Due to the same balancing currents discussed in section 3.1, the PL-based j_{sc} image does not show a significantly higher resolution than the ILIT-based method. All considerations concerning spatial resolution of ILIT also hold for DLIT.

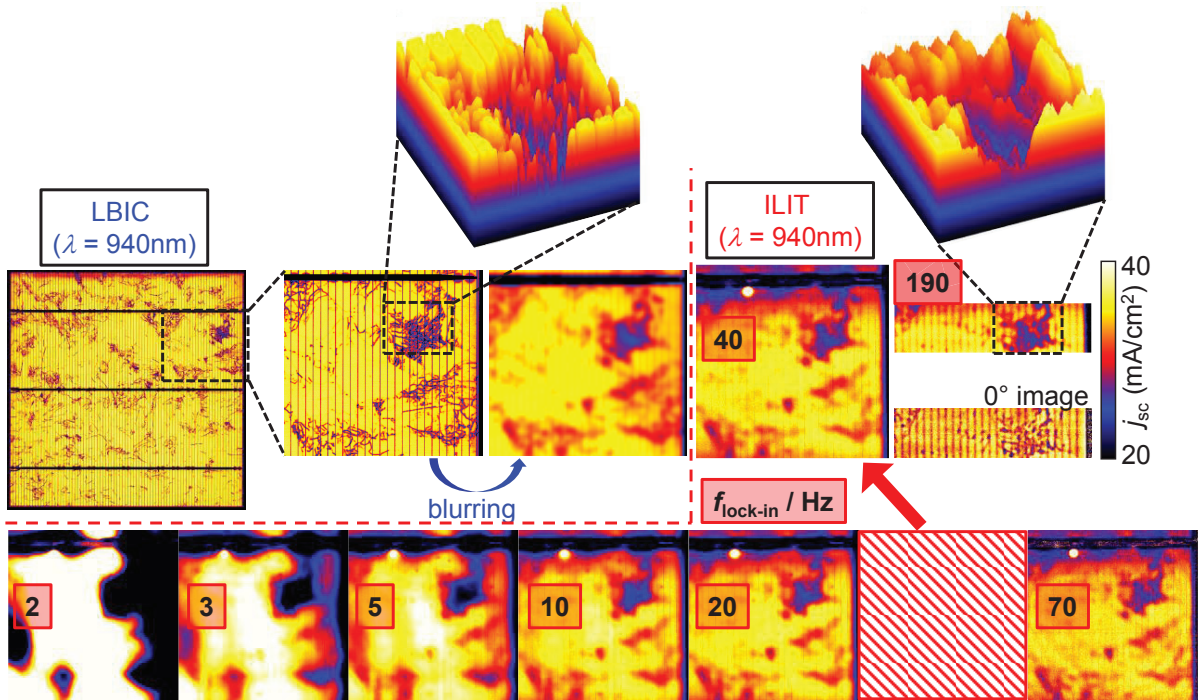


Fig. 5. Zoom into the area containing the extended dislocation cluster marked in Fig. 2. For the ILIT-based method, the lock-in frequency $f_{\text{lock-in}}$ has been varied. For $f_{\text{lock-in}} = 190$ Hz, besides the j_{sc} image (top), also the 0° image of the differential ILIT image is depicted (bottom).

3.4. Experimental freedom in spectral excitation and robustness concerning spatially varying photogeneration

As discussed in the previous sections, different scaling has been necessary to visually compare LBIC maps recorded at $\lambda = 940$ nm (\triangleq ILIT) and $\lambda = 780$ nm (\triangleq PL). The reason for this is differences in spectral response. This and the next section shall emphasize the importance of optical excitation conditions to the resulting j_{sc} images and discuss the experimental freedom of the four compared methods to choose them.

Fig. 6 shows LBIC maps for four different wavelengths of cell 2 – cast-mono, PERC SiO_2 – and a j_{sc} image for AM1.5G spectrum which has been derived from spectral integration of these four and another two LBIC maps at $\lambda = 405$ nm and $\lambda = 1060$ nm, compare section 2.4. The higher the excitation wavelength the higher is the penetration depth of the illuminated photons and, therefore, the impact of the recombination in the bulk and at the rear surface on spectral response. This can be seen in the increasing relative importance of dislocations on the displayed j_{sc} images with increasing excitation wavelength. The boxed area marks one area with differing grain orientation on the surface of the cast-mono substrate. Due to the applied alkaline texture, the reflectance in this region significantly differs from most of the other areas of the cell, which is most pronounced in the blue and red regime as illustrated by the LBIC maps. This difference in reflectance leads to a lateral variation in generated current density j_{gen} . Since the DLIT- and the PL-based methods assume j_{gen} to be constant across the entire cell, these regions are not adequately accounted for as illustrated in Fig. 6. The ILIT-based method does not assume this prerequisite and, therefore, correctly considers the impact of spatially varying j_{gen} on local j_{sc} .

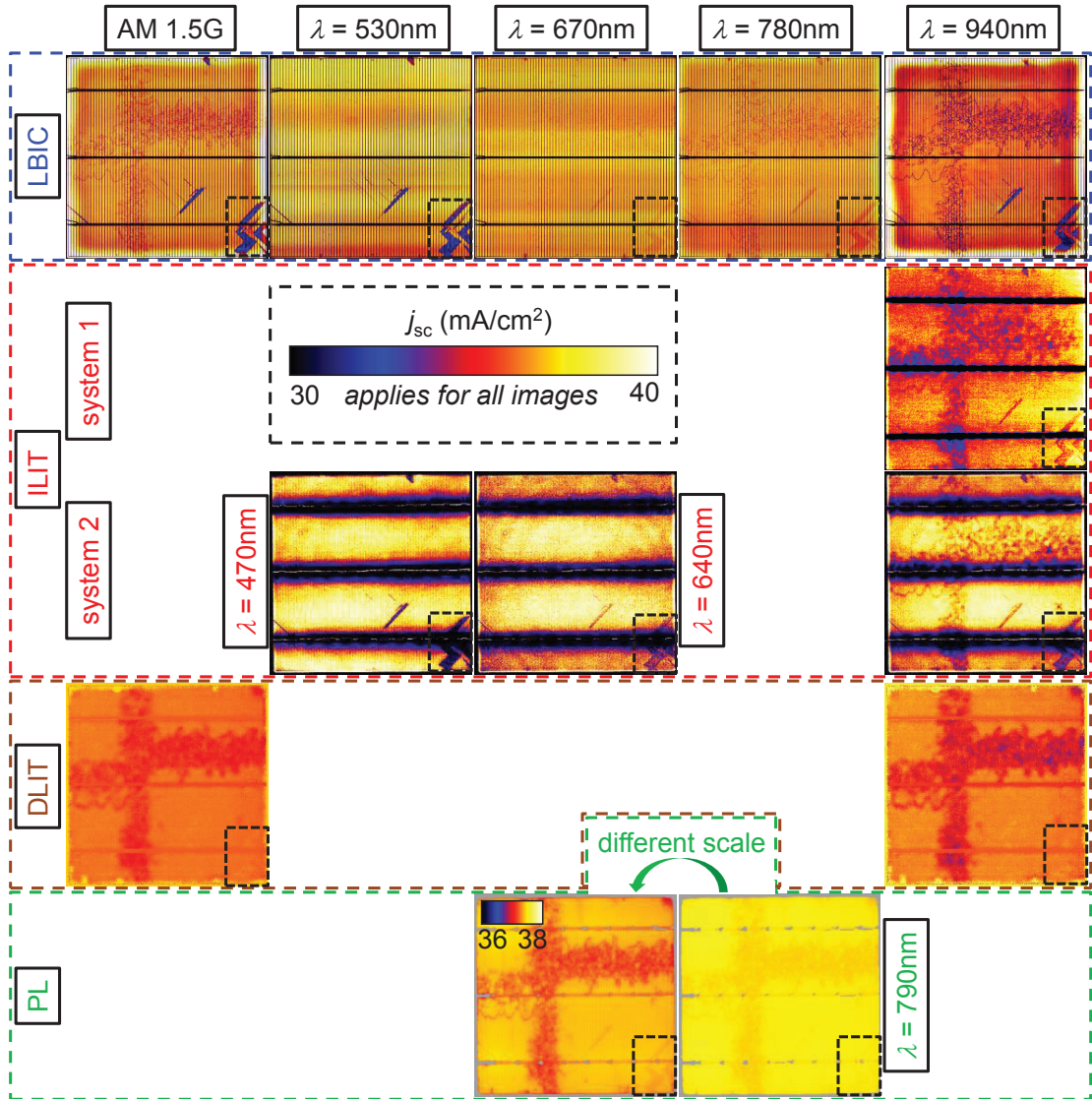


Fig. 6. Resulting j_{sc} images of cell 2 (cast-mono, PERC SiO_2) for the different methods with varying spectral excitation conditions. Box = Area with different crystal orientation and, therefore, varying reflectance and photogeneration.

In contrast to cell 1, cell 2 does not show artefacts in the PL-based j_{sc} image since it does not contain areas of significantly increased R_s or dislocation clusters with very low charge carrier lifetimes. However, the lower contrast compared with the other methods remains. Since the contrast in j_{sc} increases with increasing wavelength, the difference in excitation wavelengths (LBIC: $\lambda = 780\text{ nm}$, PL: $\lambda = 790\text{ nm}$) is not the root cause for this behaviour, but balancing currents and the assumption of a terminal-connected diode model as discussed in section 3.1. For PL, in principle any irradiation spectrum could be applied, except irradiation close to the luminescence radiation when applying a Si-CCD detector, or - technically more relevant – beyond the attenuation band of the filter, which is placed in front of the camera. Since the cameras applied during LIT are sensible in the mid-IR range and the illumination can be kept constant during application of the ILIT-based method, any practically relevant illumination source with arbitrary spectrum such as a sun simulator for AM1.5G can be used. As discussed in section 2.2, ILIT

system 2 features LED arrays at three different wavelengths. Fig. 6 shows j_{sc} images for illumination with these wavelengths, which correlate closely to the corresponding LBIC images. Due to the higher shading induced by the optical system applied in system 2 compared with the other measurement setups and the same applied scaling procedure (I_{sc} measured with system 1 as reference), the resulting j_{sc} images appear slightly brighter. For the DLIT-based method, the argument of experimental freedom in spectral excitation does not apply. The difference in optical excitation is considered by the empirical fit parameters A and B [8]. Fig. 6 shows results applying the same fit parameters extracted for the mc-Si Al-BSF cell 1 and the same scaling correction due to busbar contributions. It can be seen that the contrast is slightly lower compared with LBIC, which is most likely caused by the different cell structure and base material compared with cell 1. The significantly increased LBIC signal at the edges for the $\lambda = 780$ nm and $\lambda = 940$ nm maps that also shows in the derived AM1.5G map will be discussed in more detail in the next section.

3.5. Robustness concerning injection-dependent recombination

As shown in Fig. 6, the areas close to the edges of cell 2 – PERC, SiO_2 – show a significantly increased LBIC signal for increasing wavelengths, which has not been observed on cell 1 with an Al-BSF. In order to investigate a potential impact of the dielectric rear-side passivation in more detail, cells 3 and 4 with thermal-oxide and aluminium-oxide passivated rear sides, respectively, are investigated, which have been processed on neighbouring mc-Si substrates. Fig. 7 shows resulting j_{sc} images for the two cells (PL is again scaled in a way that LBIC images at $\lambda = 940$ nm and $\lambda = 780$ nm appear similarly). The identical grain and dislocation structures leading to a variation in local j_{sc} in both cells can be clearly seen. The pronounced increase around the edges that has also been observed for cell 2 only shows in the LBIC maps of the thermal-oxide passivated cell. It neither shows in any of the images of the aluminium-oxide passivated cell nor in the images of the thermal-oxide passivated cell determined with the other methods.

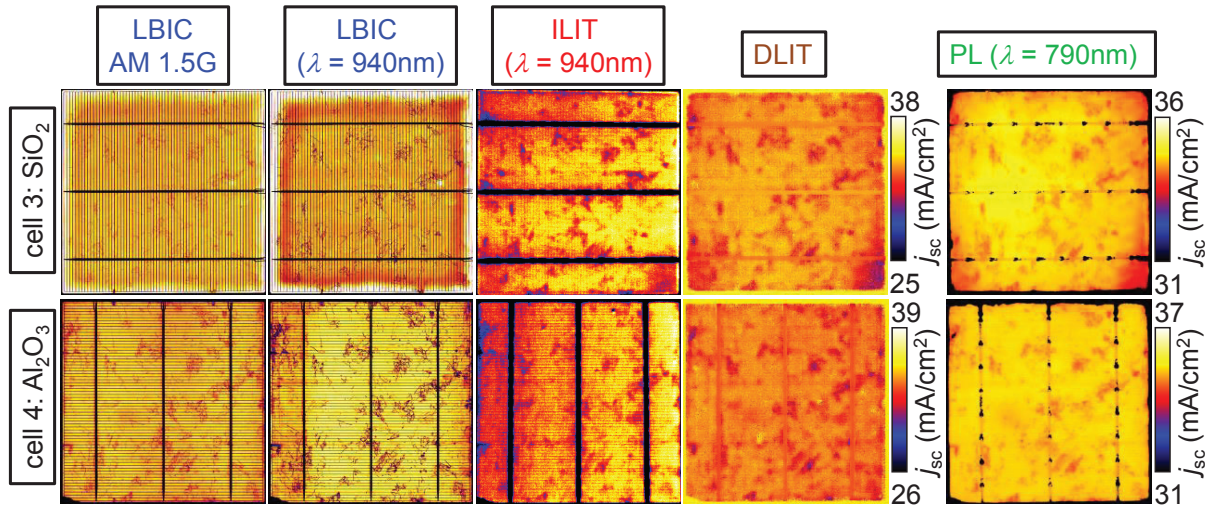


Fig. 7. Resulting j_{sc} images of cells 3 (mc-Si, PERC SiO_2) and 4 (mc-Si, PERC Al_2O_3) for the different methods.

To investigate this effect in more detail, bias-light-dependent spectral response measurements have been performed in a position at the edge and a position in the middle of the cell as indicated in Fig. 8. The resulting values of external quantum efficiency EQE for no bias light and an equivalent of 0.3 suns are displayed in Fig. 8. For bias light with intensities larger than 0.3 suns, EQE has not changed significantly anymore. It can be seen that both cells show a bias-dependence in EQE for wavelengths of $\lambda > 700$ nm, with the impact for cell 3 (SiO_2) being

significantly more pronounced. For cell 4 (Al_2O_3), the bias-dependence is very similar in the edge and the middle position, see ratios between 0.3 suns and no bias light in Fig. 8. If this holds for the entire cell, the scaling simply needs to be adjusted accordingly with a constant calibration factor. For cell 3 on the contrary, the bias-dependence is significantly different between the edge and the middle position, see Fig. 8. While for no bias light, the edge position exhibits a higher EQE than the middle position, the opposite holds for a bias light of 0.3 suns. Since the applied LBIC setup does not feature a bias light, the intensities are so low that the edge regions appear to exhibit a higher EQE than the middle regions. Since the same scaling factor is assumed for the entire cell, the edge regions therefore appear to exhibit a higher EQE and, therefore, j_{sc} although the opposite is the case for illumination intensities of 0.3 suns and higher. Fig. 8 shows the ratios between 0.3 suns and no bias light for cell 3. At $\lambda = 940$ nm, the difference is about 10 %, which needed to be considered in different calibration factors for the edge and middle regions of cell 3.

Beyond the varying carrier injection level and therefore recombination properties for very low illumination intensities as during LBIC without bias light, the injection level within the base of a solar cell varies up to two or three orders of magnitude between SC and open-circuit (OC) conditions for 1 sun illumination. When recombination properties change injection-dependently, the operating points considered for extraction of j_{sc} need to be carefully considered. As discussed in section 2.3, the DLIT-based method assumes a fixed correlation between j_{01} (\approx OC conditions) and j_{DL} (SC conditions) to extract values of local j_{sc} . If the injection-dependencies of the recombination properties vary laterally across the cell, quantitative differences will be the consequence in analogy to the case discussed for LBIC above: Different calibration factors needed to be applied to overcome this restraint. Problems related to injection-dependent recombination become even more pronounced for the PL-based method since it assumes low-level injection to hold in all recorded images, including one close to OC at 1 sun [13]. If a bias light can be applied during LBIC, it should map j_{sc} under realistic conditions. The ILIT-based method is not affected by injection-dependent recombination since it measures the investigated cell under global SC conditions of the entire cell.

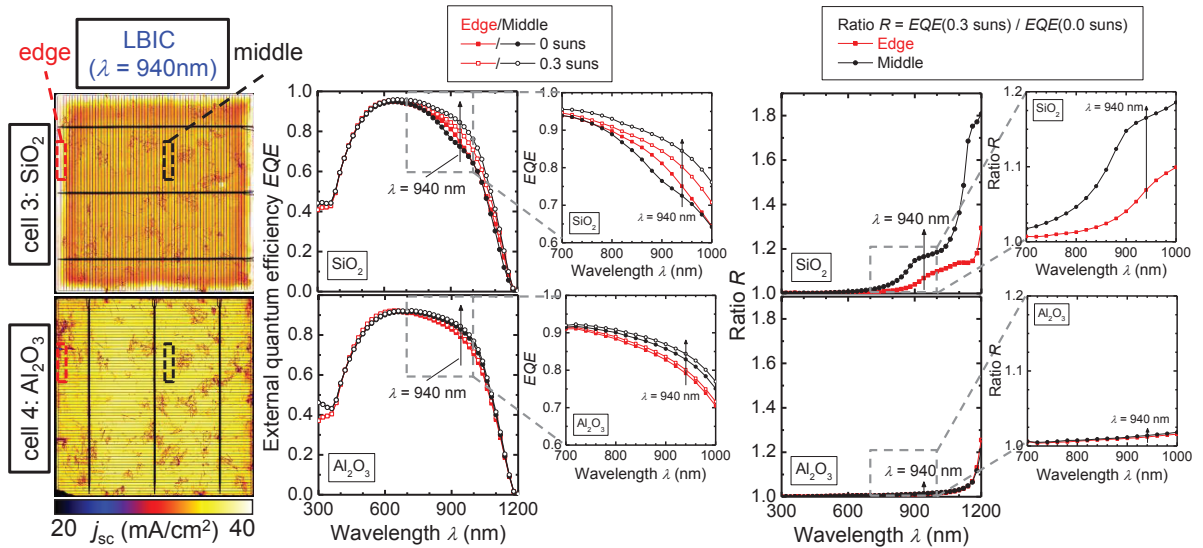


Fig. 8. LBIC maps of cells 3 (SiO_2) and 4 (Al_2O_3) at $\lambda = 940$ nm and results of bias-dependent external quantum efficiency measurements at two positions at the edge and in the middle of the cells, respectively, indicated by boxes in the LBIC maps.

3.6. Measurement time and direct applicability to methods imaging other diode model parameters

As mentioned in section 2, LBIC is a mapping technique while the LIT- and PL-based methods are imaging techniques applying cameras. Hence, the measurement time of LBIC highly depends on the sample size and the

chosen step width (\triangleq resolution) during mapping. Typically, the measurement time for a highly resolved large-area measurement as discussed in this work is in the order of hours. However, if light sources such as laser diodes with differing emission wavelengths can be modulated at different frequencies, spectrally-resolved (SR-) LBIC maps can be generated without significantly increasing measurement time [1,20]. For lock-in thermography as for any lock-in based measurement technique, the signal-to-noise ratio gets the higher, the longer the measurement is integrated. During ILIT, comparably small signals need to be detected within a high background signal due to the applied illumination, while DLIT detects comparably large changes within a low background signal. Hence, DLIT generally requires shorter integration times than ILIT which, however, depends on the operating points in detail. On the other hand, one image may be sufficient for the ILIT-based approach while the DLIT-based approach requires at least two. Since every LIT system exhibits its inherent noise level (mainly determined by the camera), it is difficult to state general required measurement times for the discussed methods. The measurement times for the LIT images discussed within this work have been in the order of minutes to a maximum of about half an hour. Despite the comparably high number of required images for the PL-based method, compare Tab. 2, PL is by far the fastest of the considered methods with measurement times in the order of seconds for each image.

In principle, all j_{sc} images could be combined with any reported local solar cell parameter imaging method by, e.g., adequate blurring of the LBIC map or deconvolution of LIT- and PL-based images of the other parameters. The most self-suggesting application to use the ILIT- or DLIT-based methods would be in conjunction with DLIT-based local efficiency imaging [5,16]. The implied voltage based PL evaluation [6] already includes the assumption of a non-uniform short-circuit current density.

3.7. Summary

Table 3 shows a summary of the addressed points with a subjective rating of the strengths and weaknesses of each method. As can be seen, each method has its advantages and disadvantages and the suitability depends on the requirements of the user. The authors draw the arguable conclusion that LBIC and the ILIT-based method exhibit the highest accuracy of the investigated methods. When well-calibrated, the DLIT-based method has also shown very accurate in most of the cell area while the PL-based method has persistently resulted in decreased contrast in quantitative local j_{sc} .

It needs to be stated that this work only considers “classical” Al-BSF and dielectrically passivated solar cells with a full-area front-side emitter on *p*-type silicon. The rating may differ for other cell concepts such as interdigitated back-contact (IBC), heterojunction cells, emitter-wrap-through (EWT [31]) or both sides collecting and contacted (BOSCO [32]) or solar cells manufactured on other materials than silicon. Especially, two-dimensional cell concepts that are not well described with a one-diode model and that exhibit significantly deviating current paths in the dark and under illumination would be interesting to include into future work on this matter.

Table 3. Strengths and weaknesses (++ / + / 0 / - / - -) of the discussed j_{sc} imaging methods.

Category	LBIC	ILIT	DLIT	PL
Accuracy	+	+	0	-
Measurement time	--	0	0 / -	++
Spatial resolution	++	-	-	0 / -
Experimental freedom in spectral excitation	++	+	n.a.	0
Self-consistent calibration	0	+	0	+ / 0
Robustness concerning locally increased R_s	+	+	+ / 0	-
Robustness concerning injection-dependent recombination	0 / -	+	0 / -	-
Robustness concerning spatially varying photogeneration	++	+	-	-
Robustness concerning algorithm artefacts	+	++	+	-
Direct applicability to methods imaging other diode model parameters	-	+	++	++

4. Conclusion

Within this work, three recently proposed short-circuit current density imaging methods based on illuminated lock-in thermography (ILIT), dark lock-in thermography (DLIT) and photoluminescence (PL) imaging have been compared in theory and by experiment. As a reference, the established method of spectrally-resolved light-beam induced current (SR-LBIC) mapping has been considered. The methods have been applied to silicon solar cells with different substrate materials and rear-side passivation schemes. The results are compared in terms of measurement time, spatial resolution, experimental freedom in spectral excitation, self-consistent calibration, direct applicability to techniques imaging other solar cell parameters and robustness concerning locally increased series resistance, injection-dependent recombination, spatially varying photogeneration and algorithm artefacts. While each method has its strengths and weaknesses and the suitability depends on the requirements of the user, the subjective result of the authors is that LBIC and ILIT result in the most accurate result, closely followed by well-calibrated DLIT. PL has shown to result in lower contrast in quantitative local j_{sc} values due to the general invalidity of the underlying terminal-connected diode model. However, the PL-based method is still valuable to increase the accuracy of local efficiency imaging via luminescence imaging, especially due to its outstandingly short measurement times compared with the other methods.

Acknowledgements

The authors acknowledge Elisabeth Schäffer for SR-LBIC and QE measurements and Sven Wasmer for ILIT measurements.

References

- [1] W. Warta, J. Sutter, B. F. Wagner, R. Schindler, "Impact of Diffusion Length Distribution on the Performance of mc-Silicon Solar Cells"; in Proceedings of the 2nd World Conference and Exhibition on Photovoltaic Solar Energy Conversion, Vienna, Austria, pp. 1650–1653, 1998.
- [2] M. Padilla, B. Michl, B. Thaidigsmann, W. Warta, M. C. Schubert, "Short-circuit current density mapping for solar cells", *Solar Energy Materials and Solar Cells*, Vol. 120, pp. 282–288, 2014.
- [3] B. Michl, M. Rüdiger, J. A. Giesecke, M. Hermle, W. Warta, M. C. Schubert, "Efficiency limiting bulk recombination in multicrystalline silicon solar cells", *Solar Energy Materials and Solar Cells*, Vol. 98, pp. 441–447, 2012.
- [4] C. Shen, H. Kampwerth, M. A. Green, "Spatially resolved photoluminescence imaging of essential silicon solar cell parameters"; in Proceedings of the 38th IEEE Photovoltaic Specialists Conference, Austin, TX, USA, pp. 001855–001859, 2012.
- [5] O. Breitenstein, "Local efficiency analysis of solar cells based on lock-in thermography", *Solar Energy Materials and Solar Cells*, Vol. 107, pp. 381–389, 2012.
- [6] O. Breitenstein, H. Höfller, J. Haunschild, "Photoluminescence image evaluation of solar cells based on implied voltage distribution", *Solar Energy Materials and Solar Cells*, Vol. 128, pp. 296–299, 2014.
- [7] F. Fertig, J. Greulich, S. Rein, "Spatially Resolved Determination of the Short-Circuit Current Density of Silicon Solar Cells via Lock-In Thermography", *Appl. Phys. Lett.*, Vol. 104, p. 201111, 2014.
- [8] O. Breitenstein, F. Fertig, J. Bauer, "An empirical method for imaging the short circuit current density in silicon solar cells based on dark lock-in thermography", *Solar Energy Materials and Solar Cells*, submitted for publication, 2015.
- [9] O. Breitenstein, "An Alternative One-Diode Model for Illuminated Solar Cells", *IEEE J. Photovoltaics*, Vol. 4, No. 3, pp. 899–905, 2014.
- [10] T. Trupke, E. Pink, R. A. Bardos, M. D. Abbott, "Spatially resolved series resistance of silicon solar cells obtained from luminescence imaging", *Appl. Phys. Lett.*, Vol. 90, No. 9, p. 093506, 2007.
- [11] M. Glatthaar, J. Haunschild, M. Kasemann, J. Giesecke, W. Warta, S. Rein, "Spatially resolved determination of dark saturation current and series resistance of silicon solar cells", *phys. stat. sol. (RRL)*, Vol. 4, No. 1-2, pp. 13–15, 2010.
- [12] M. Glatthaar, J. Haunschild, R. Zeidler, M. Demant, J. Greulich, B. Michl, W. Warta, S. Rein, R. Preu, "Evaluating luminescence based voltage images of silicon solar cells", *J. Appl. Phys.*, Vol. 108, No. 1, p. 014501, 2010.
- [13] H. Höfller, O. Breitenstein, J. Haunschild, "Short-Circuit Current Density Imaging Via PL Image Evaluation Based on Implied Voltage Distribution", *IEEE J. Photovoltaics*, Vol. 5, No. 2, pp. 613–618, 2015.
- [14] O. Breitenstein, W. Warta, M. Langenkamp, "Lock-in thermography", Springer, Heidelberg, New York, 2010.
- [15] F. Fertig, J. Greulich, S. Rein, "Short-circuit current density imaging of crystalline silicon solar cells via lock-in thermography: Robustness and simplifications", *J. Appl. Phys.*, Vol. 116, p. 184501, 2014.
- [16] O. Breitenstein, "Nondestructive local analysis of current–voltage characteristics of solar cells by lock-in thermography", *Solar Energy Materials and Solar Cells*, Vol. 95, No. 10, pp. 2933–2936, 2011.

- [17] C. H. Seager, "The determination of grain-boundary recombination rates by scanned spot excitation methods", *J. Appl. Phys.*, Vol. 53, No. 8, p. 5968, 1982.
- [18] J. Marek, "Light-beam-induced current characterization of grain boundaries", *J. Appl. Phys.*, Vol. 55, No. 2, p. 318, 1984.
- [19] M. Stemmer; S. Martinuzzi, "Mapping of local minority carrier diffusion length applied to multicrystalline silicon cells"; in Proceedings of the 11th E. C. Photovoltaic Solar Energy Conference, Montreux, Switzerland, pp. 450–452, 1992.
- [20] W. D. Sawyer, "An improved method of light-beam-induced current characterization of grain boundaries", *J. Appl. Phys.*, Vol. 59, No. 7, p. 2361, 1986.
- [21] A. W. Blakers, A. Wang, A. M. Milne, J. Zhao, M. A. Green, "22.8% efficient silicon solar cell", *Appl. Phys. Lett.*, Vol. 55, No. 13, p. 1363, 1989.
- [22] S. Mack, U. Jager, G. Kastner, E. A. Wotke, U. Belledin, A. Wolf, R. Preu, D. Biro, "Towards 19% efficient industrial PERC devices using simultaneous front emitter and rear surface passivation by thermal oxidation"; in Proceedings of the 35th IEEE Photovoltaic Specialists Conference, Honolulu, HI, USA, pp. 000034–000038, 2010.
- [23] E. Schneiderlöchner, R. Preu, R. Lüdemann, S. W. Glunz, "Laser-fired rear contacts for crystalline silicon solar cells", *Prog. Photovolt: Res. Appl.*, Vol. 10, No. 1, pp. 29–34, 2002.
- [24] P. Saint-Cast, D. Kania, M. Hofmann, J. Benick, J. Rentsch, R. Preu, "Very low surface recombination velocity on p-type c-Si by high-rate plasma-deposited aluminum oxide", *Appl. Phys. Lett.*, Vol. 95, No. 15, p. 151502, 2009.
- [25] M. Kasemann, B. Walter, C. Meinhardt, J. Ebser, W. Kwapil, W. Warta, "Emissivity-corrected power loss calibration for lock-in thermography measurements on silicon solar cells", *J. Appl. Phys.*, Vol. 103, No. 11, p. 113503, 2008.
- [26] B. Michl, D. Impera, M. Bivour, W. Warta, M. C. Schubert, "Suns-PLI as a powerful tool for spatially resolved fill factor analysis of solar cells", *Prog. Photovolt: Res. Appl.*, Vol. 22, No. 5, pp. 581–586, 2014.
- [27] H. Höffler, H. Al-Mohtaseb, J. Haunschild, B. Michl, M. Kasemann, "Voltage calibration of luminescence images of silicon solar cells", *J. Appl. Phys.*, Vol. 115, No. 3, p. 034508, 2014.
- [28] O. Breitenstein, J. Bauer, D. Hinken, K. Bothe, "The reliability of thermography- and luminescence-based series resistance and saturation current density imaging", *Solar Energy Materials and Solar Cells*, Vol. 137, pp. 50–60, 2015.
- [29] M. Padilla et al., "Manuscript in preparation".
- [30] K. Ramspeck, K. Bothe, D. Hinken, B. Fischer, J. Schmidt, R. Brendel, "Recombination current and series resistance imaging of solar cells by combined luminescence and lock-in thermography", *Appl. Phys. Lett.*, Vol. 90, No. 15, p. 153502, 2007.
- [31] J. M. Gee, W. K. Schubert, P. A. Basore, "Emitter wrap-through solar cell"; in Record of the Twenty Third IEEE Photovoltaic Specialists Conference, Louisville, KY, USA, pp. 265–270, 1993.
- [32] F. Fertig, K. Krauß, J. Greulich, F. Clement, D. Biro, R. Preu, S. Rein, "The BOSCO solar cell - a both sides collecting and contacted structure", *phys. stat. sol. (RRL)*, Vol. 8, pp. 381–384, 2014.